Characterization of cardiac-induced noise in R_2* maps of the brain

Quentin Raynaud[1], Giulia Di Domenicantonio[1], Jérôme Yerly[2,3], Thomas Dardano[1], Ruud B. van Heeswijk[2], Antoine Lutti[1]

[1]*Laboratory for Research in Neuroimaging, Department for Clinical Neuroscience, Lausanne University Hospital and University of Lausanne, Lausanne, Switzerland*

[2]*Department of Diagnostic and Interventional Radiology, Lausanne University Hospital and University of Lausanne, Lausanne, Switzerland.*

[3]*Center for Biomedical Imaging (CIBM), Lausanne, Switzerland.*

Correspondence

Quentin Raynaud

Laboratory for Research in Neuroimaging, Department for Clinical Neuroscience, Lausanne University Hospital, Ch. de Mont-Paisible 16, CH-1011 Lausanne

Email: quentin.raynaud@chuv.ch

Abstract

Purpose

Cardiac pulsation increases the noise level in brain maps of the MRI parameter R_2*. Cardiac-induced noise is challenging to mitigate during the acquisition of R_2* mapping data because the characteristics of this noise remain largely unknown. In this work, we characterize cardiac-induced noise in brain maps of the MRI parameter R_2*.

Methods

We introduce a sampling strategy that enables the acquisition of multi-echo data in several intervals of the cardiac cycle. From this data, we estimate the variability of brain R_2* maps due to cardiac-induced fluctuations and identify the most sensitive area of k-space. From these characteristics, we derive a novel sampling strategy that successfully mitigates cardiac-induced noise in R_2* maps of the brain.

Results

In inferior brain regions, cardiac pulsation accounts for R_2* variations of up to $3s^{-1}$ across the cardiac cycle, i.e. ~35% of the overall variability. Cardiac-induced fluctuations occur throughout the cardiac cycle and exhibit a reduced intensity during the first quarter of the cycle after the detection of the systole at the finger. 50-60% of the overall cardiac-induced noise is contained near the k-space centre ($k < 0.074\ mm^{-1}$), corresponding to 22% of voxels at 4mm resolution. The proposed cardiac noise mitigation strategy reduces the variability of R_2* estimates across repetitions by 11% in the brainstem and 6% across the whole brain.

Conclusion

We provide characteristics of cardiac-induced noise in brain maps of the MRI parameter R_2* that constitute a basis for the design of mitigation strategies during data acquisition.

Keywords:

Brain; cardiac-induced noise; Physiological noise; quantitative MRI; R2*; MRI relaxometry;

1. Introduction

MRI relaxometry consists in estimating the value of the MRI parameters that drive signal intensities in MR images[1–3]. Relaxometry data exhibit a lower dependence on acquisition parameters and scanner hardware than conventional structural MRI data, leading to increased reproducibility in multi-centre studies[4,5]. Maps of the transverse relaxation rate (R_2* =1/T_2^*) are computed from gradient-echo MR images acquired at multiple echo times. R_2* is driven by spin-spin interactions and microscopic magnetic field inhomogeneities that arise from magnetic material within the tissue[6,7]. Therefore, R_2* correlates with iron and myelin concentration in brain tissue[8–11] and enables the monitoring of disease evolution in Parkinson's disease[12,13], multiple sclerosis[14] and Alzheimer's disease[15].

Cardiac pulsation leads to instabilities in brain MRI data that reduce the sensitivity of R_2* estimates to brain disease in neuroscience studies. Cardiac pulsation gives rise to a systolic pressure wave that reaches the brain ~50ms after onset of the R-wave in an electrocardiogram[16,17], and 30-130ms prior to the detection of the systolic peak with a pulse oximeter attached to the finger[18–20]. This wave results in pulsatile brain motion due to the expansion of blood vessels[21], variations in blood flow velocity[17,22–24], brain tissue deformation[25–28], CSF motion[29–31], bulk head motion[32] and change in O_2/CO_2 concentrations[33,34]. The brain areas primarily affected by cardiac pulsation are inferior brain regions close to large vessels such as the brainstem[35], cerebellum[36] and orbitofrontal cortex[31,37], highly vascularized grey matter regions[31] and brain regions near the ventricles[37,38]. The effects of cardiac pulsation on MR images arise from the interaction of spin displacements with the amplitude and direction of the gradients of magnetic fields used for image encoding[39]. While laminar flow leads to a net phase shift in MRI data, turbulent or anisotropic flow across an image voxel leads to a distribution of spin phase that results in a net loss in signal amplitude[35]. Cardiac pulsation reduces the BOLD sensitivity of functional MRI data[31,34,35] and leads to bias in measures of the apparent diffusion coefficient[27] which can be corrected from the recording of cardiac pulsation concurrently with the MRI data[40–43].

R_2* relaxometry is performed with oscillating, high-amplitude readout gradients. Because the coupling between encoding gradients and cardiac pulsation accumulates over time[39], cardiac-induced signal intensity loss is expected to increase with the echo time, leading to exponential-like effects i.e. bias of the R_2* estimates. Furthermore, because data acquisition takes place over several minutes, raw k-space data points may show variable levels of cardiac-induced noise, leading to aliasing artifacts in the reconstructed images[44,45]. Few data acquisition strategy currently exists that mitigate cardiac-induced noise in R_2* maps of the brain. On the model of diffusion acquisitions[18,19], such strategies might include adjusting k-space sampling in real-time according to patients' cardiac pulsation, or averaging across multiple data samples in the sensitive areas of k-space. However, these strategies all hinge on a detailed description of cardiac-induced noise in brain relaxometry data that is currently not available.

Here, we provide a complete assessment of cardiac-induced noise in R_2* relaxometry data of the brain. We introduce an optimized sampling strategy that enables the acquisition of multi-echo k-space data in several intervals of the cardiac cycle, and allows to resolve the effect of cardiac pulsation on the MR signal ('*cardiac-induced noise*'). From this data, we provide estimates of the variability of R_2* maps of the brain across the cardiac cycle and identify the fraction of k-space that is sensitive to cardiac-induced fluctuations. From these results, we derive a novel sampling strategy that successfully mitigates cardiac-induced noise in R_2* maps of the brain.

2. Methods

2.1. Characterization of R_2* changes across the cardiac cycle

In order to analyse the effects of cardiac pulsation on brain R_2* maps, multi-echo gradient echo data were acquired across the cardiac cycle and distributed over five-dimensions (three spatial dimensions, echo time, phase of the cardiac cycle). Cardiac-induced fluctuations were then modelled by Fourier series decomposition of the k-space signal change across the cardiac cycle. From the modelled cardiac-induced fluctuations we 1) measured the amplitude of cardiac-induced noise in R_2* maps of the brain and 2) analysed the distribution of cardiac-induced noise in k-space to identify sensitive regions.

2.1.1. 5D data sampling strategy

The sampling strategy for the acquisition of the five-dimensional data was inspired by recent developments in high-dimensional heart and brain imaging[22,46–49] where the cardiac cycle is resolved by pooling k-space data from multiple heartbeats into their respective cardiac phases ('*cardiac bins*'). Multi-echo data was acquired continuously for 1 hour while the cardiac rhythm of the participants was being recorded using a pulse-oximeter attached to the finger. Acquisition of the MRI data was not synchronized with the heart rates of the participants. The data was binned retrospectively according to the phase of the cardiac cycle at the time of its acquisition, leading to datasets with three spatial dimensions (readout and two phase encoding directions), one echo-time dimension and one cardiac phase dimension (Figure 1A). We used 12 bins for the cardiac cycle from the trade-off between resolving the systolic period (~300ms duration[16,31]) and obtaining sufficient k-space data in each bin for routine image reconstruction. The cardiac phase was set to zero at the peak of the pulse-oximeter signal.

Data was acquired linearly within a predefined kernel, i.e. a subset of k-space along the two phase encoding directions. The kernel size was optimized to mitigate spurious effects such as head-motion, breathing or swallowing, and minimize the occurrence of k-space data points with empty cardiac bins (see Appendix). 30 samples were acquired at each k-space location. Multiple samples from the same cardiac bin were averaged, and the data in missing cardiac bins were linearly interpolated from the neighbouring bins.

Images for each echo and cardiac bin were reconstructed using SENSE[50] with an acceleration factor of 1. The raw 5D images contained signal from areas outside and below the brain (e.g. tongue, mouth, neck) along the readout encoding direction (orientation: head-feet). Noise from these areas might alias in the 2D plane of the two phase encoding directions but cannot alias into the brain along the readout direction due to the high readout bandwidth. Therefore, this noise is of no interest for the characterization of cardiac-induced noise in brain images and the raw 5D images were trimmed below the medulla along the readout direction.

2.1.2. Modelling of cardiac-induced signal fluctuations

Modelling of cardiac-induced signal fluctuations was performed in k-space. Similar to RETROKCOR[40,41], we modelled the fluctuations of the real and imaginary parts of the MRI signal across the cardiac cycle using Fourier series of sinusoidal basis functions with a fundamental frequency and its first harmonic (Figure 2A). This analysis was conducted at each k-space location separately.

2.1.3. Characterization of R_2* changes across the cardiac cycle

To specifically assess the effect of cardiac pulsation on R_2* estimates, we only considered the changes of the multi-echo data across the cardiac cycle that were modelled as cardiac-induced fluctuations (see section 2.1.2). R_2* maps were computed after Fourier transform of the data, from the regression of the log signal with the corresponding echo times[51] (Figure 1B). The noise level on the R_2* estimates was calculated as the root-mean-squared error (RMSE) between the MR signal and the R_2* fit.

2.1.4. Determination of the k-space regions sensitive to cardiac-induced fluctuations

To identify the region of k-space sensitive to cardiac pulsation, the modelled cardiac-induced fluctuations were removed from a circular area of k-space in the plane of the two phase encoding directions centred on the origin ('*detrending*'). R_2* maps were computed from the resulting data for each bin of the cardiac cycle as described in 2.1.3, that contained cardiac-induced noise from the peripheral region of k-space only. The process was repeated while increasing the radius of the detrending area to include from 0% to 100% of k-space, in steps of 2%.

Subsequent analyses of these results were based on the decrease of the standard deviation (SD) of the R_2* maps across the cardiac cycle with increasing radius of the detrending area. In order to study the distribution of the modelled cardiac-induced noise in k-space, only the contribution of the modelled cardiac-induced noise to R_2* variability was considered. In order to measure the level of cardiac-induced noise compared to the overall noise, the contribution of all noise sources was included by considering the variability of the original R_2* mapping data.

2.2. Informed cardiac-induced noise mitigation strategy

To illustrate how characteristics of cardiac-induced noise can inform a choice of noise mitigation strategy for data acquisition, we implemented a cardiac gating strategy widely used in diffusion MRI[18–20] that involves suspending data acquisition during detrimental periods of the cardiac cycle. Our implementation of cardiac gating for 3D Fast low angle shot (FLASH) sequences maintained RF excitation during periods of suspension to preserve the steady state of the magnetization[52]. The time window for data acquisition was the period of the cardiac cycle with the least cardiac-induced noise (figure 2C). To minimize the increase in scan time due to the suspension of data acquisition, cardiac gating was only implemented for the acquisition of the subset of k-space that contains most of the cardiac-induced noise (figure 5B).

In order to assess the efficiency of the proposed strategy to mitigate cardiac-induced noise, we compared the SD of R_2* and RMSE maps across multiple repetitions from data acquired with and without cardiac gating.

2.3. MRI protocols

Data acquisition was performed on a clinical 3T scanner (Magnetom Prisma, Siemens Healthcare, Erlangen, Germany) equipped with a 64-channel head-neck coil. Multi-echo Cartesian R_2* mapping data was acquired using a custom-made 3D FLASH sequence. 15 echo images were acquired with a bipolar readout[4] (repetition time TR=40ms; echo times TE=2.34ms to 35.10ms with 2.34ms spacing, RF excitation flip angle = 16°). The readout direction was kept along the head-feet direction.

All protocols included an MPRAGE[53] image for segmentation and anatomical reference (1mm^3 isometric resolution, TR/TE = 2000/2.39ms, GRAPPA[54] acceleration factor 2 with 24 reference lines, RF excitation flip angle = 9°). The acquisition time was 4:16 minutes.

2.3.1. Five-dimensional dataset for the characterization of cardiac-induced noise

Image resolution was 2mm along the readout direction and 4mm along the phase-encode directions. This was deemed sufficient to fully capture cardiac-induced fluctuations because physiological noise scales with signal amplitude and is strongly reduced in high k-space regions[41].

One preliminary dataset was acquired on one female participant (31 years old) to determine the kernel size optimal for the mitigation of spurious effects such as swallowing on the characterization of cardiac-

induced noise (see appendix). For this dataset, 30 data samples were acquired consecutively at each k-space location.

Following kernel optimization, 5D data was acquired on five adult participants (2 females, 33±7 years old) to characterize cardiac-induced noise in brain R_2* maps, using a kernel size of 30/2 along the fast/slow phase-encode directions (strategy 2 in appendix), optimal for the mitigation of spurious effects. The acquisition time was 56:21 minutes.

To compute the coil sensitivity profiles used for image reconstruction[50], two 3D FLASH datasets were acquired in each participant with 4×4×4mm^3 image resolution, with both head and body coils for signal reception (TR/TE=5.72ms/2.34ms, excitation flip angle=6°, acquisition time 16s)[55].

2.3.2. Informed cardiac-induced noise mitigation strategy

The assessment of the candidate strategy to mitigate cardiac-induced noise in R_2* maps was conducted on seven adult participants (6 females, 32±7 years old). The protocol included 6 multi-echo 3D FLASH acquisitions with a 2D linear Cartesian trajectory, including 3 scans with the proposed cardiac gating strategy. The order of the acquisitions with and without cardiac gating was randomized. The voxel size was 1×2×2mm^3, similar to brain R_2* maps acquired in clinical protocols[56–58]. The total acquisition time was 53:22 minutes.

The proposed implementation of cardiac gating only allowed data acquisition over the quarter of the cardiac cycle that followed detection of the R-wave with the pulse oximeter. To minimize the subsequent increase in scan time, cardiac gating was only effective for the acquisition of the subset of k-space that contains most of the cardiac-induced noise (figure 5). This corresponds to 22% of k-space at the resolution of the 5D acquisition (2x4x4mm^3), but only 5.5% of k-space with the resolution used here (1x2x2mm^3). The acquisition time was 8:48 and 7:34 minutes for the acquisitions with and without cardiac gating.

2.4. Image reconstruction and analysis

Image reconstruction and data analyses were performed using bespoke analysis scripts written in Matlab (version 2017a, The Mathworks, Natick, MA).

Image coregistration and segmentation were conducted using Statistical Parametric Mapping (SPM12, Wellcome Centre for Human Neuroimaging, London). The MPRAGE images were segmented into maps of grey and white matter probabilities using Unified Segmentation[59]. Whole-brain masks were computed from the grey and white matter segments and included voxels with a combined probability of 0.9 or above. As described in Lutti et al.[60], regional masks were computed from the grey matter maximum probability labels computed in the 'MICCAI 2012 Grand Challenge and Workshop on Multi-Atlas Labeling' (**https://masi.vuse.vanderbilt.edu/workshop2012/index.php/Challenge_Details**), using MRI scans from the OASIS project (**http://www.oasis-brains.org/**) and labelled data provided by Neuromorphometrics, Inc. (**http://neuromorphometrics.com/**) under academic subscription.

Masks including blood vessels were defined from the voxels with a combined grey and white matter probability below 0.1, and with a 1st-order component of the modelled cardiac-induced noise above the average brain value. This mask mostly contained voxels in the arteries and veins but also some in the CSF.

3. Results

The signal fluctuations across the cardiac cycle were modelled as cardiac-induced fluctuations using Fourier series decomposition (Figure 2A). The amplitude of the modelled cardiac-induced fluctuations

are two orders of magnitude larger at the centre of k-space than at the edges for both the real and imaginary parts of the data (Figure 2B). The global measure of cardiac-induced noise level, computed as the average signal deviation from the mean across the cardiac cycle, increases by a factor 2-2.5 with echo time and is modulated by the cardiac phase by a factor 1.5 (Figure 2C). Consistently with previous observations[16–20,61], the maximum cardiac-induced noise level occurs upon arrival of the heart systole in the brain (cardiac phase ≈ $3\pi/4$). The first quarter of the cardiac cycle shows a reduced level of cardiac-induced noise.

Variations in R_2* of up to $3s^{-1}$ take place across the cardiac cycle (Figure 3A and supplemental animation 1 and animation 2), that arise from exponential-like effects of cardiac pulsation on the MRI signal across echoes (Figure 3B). Before removal of the cardiac-induced fluctuations, the highest levels of R_2* variation across the cardiac cycle are observed in inferior brain regions such as the brainstem and cerebellum (Figure 3C). After removal, the spatial uniformity of the R_2* variations is improved. At the regional level, cardiac pulsation respectively accounts for 32%, 34%, and 44% of the overall SD in R_2* across the cardiac cycle in the brainstem, whole brain and blood vessels (Figure 3D).

The residuals of the fit (RMSE) of the MRI data with an exponential model of transverse relaxation show variations of up to 40% across the cardiac cycle (Figure 4A). The RMSE is indicative of the noise level on the R_2* estimates, and this variation reflects a noise-like effect of cardiac pulsation across echoes (Figure 4B), with a general increase of the RMSE with the echo time. Before removal of the modelled cardiac-induced fluctuations, the highest level of variation in RMSE across the cardiac cycle are observed in inferior brain regions such as the brainstem and cerebellum (Figure 4C). After removal, the spatial uniformity of the RMSE variations is improved (Figure 4D). At the regional level, cardiac pulsation respectively accounts for 28%, 30% and 43% of the overall SD of RMSE across the cardiac cycle in the brainstem, whole brain and blood vessels.

The study of the relative standard deviation of R_2* across the cardiac cycle as a function of the detrended fraction of k-space shows an inflexion point near ~80% of detrended voxels (Figure 5A). From 80 to 100% of detrended voxels, the standard deviation of R_2* across the cardiac cycle varies as the inverse of the square root of the number of remaining voxels (black curve), indicating that R_2* variability is dominated by thermal noise[62]. A knee point is apparent near the origin and delineates the region of k-space where the local variation in the level of cardiac-induced noise is sharp, i.e. the region of k-space sensitive to cardiac-induced noise. This region was estimated to include ~22-24% of the central points of k-space using the Kneedle algorithm[63] (dashed lines in Figure 5A and Figure 5B) and accounts for respectively 37/45/42/25% of the total cardiac-induced fluctuations in the brainstem/cerebellum/whole-brain/blood vessels. Figure 5C shows the standard deviation across the cardiac cycle of R_2* maps computed from the original raw data, detrended over an increasing fraction of k-space. The level of cardiac-induced noise contained in the sensitive k-space region accounts for 17/23/20/15% of the standard deviation of R_2* across the cardiac cycle in the brainstem/cerebellum/whole-brain/blood vessels respectively.

From the characteristics of cardiac-induced noise outlined above, we compared the reproducibility of R_2* maps obtained with a standard acquisition and with an implementation of cardiac gating that allows acquisition of the data sensitive to cardiac-induced noise during the first quarter of the cardiac cycle only (Figure 6A). The decrease in R_2* variability across repetitions with the CG sequence was most pronounced in inferior brain regions. The average decrease in R_2* variability was respectively 11/8/6% in the brainstem/cerebellum/whole-brain (Figure 6B). Figure 6C shows maps of the RMSE of the fit averaged across repetitions for the standard and CG sequences. Similar to R_2* variability, the decrease in RMSE with the CG sequence was most pronounced in inferior brain regions. However, aliasing of cardiac-induced noise that originate in the circle of Willis along the anterior-posterior phase encode

direction can be observed. The average decrease in RMSE was respectively 7/7/3% in the brainstem/cerebellum/whole-brain respectively (Figure 6D).

4. Discussion

We presented an extensive characterization of noise induced by cardiac pulsation in quantitative maps of the MRI parameter R_2* in the brain. Multi-echo R_2* mapping data was acquired across the cardiac cycle using a continuous sampling strategy similar to that used for high-dimensional brain and cardiac imaging[22,46–49]. Data acquisition was conducted using a sampling kernel optimized to mitigate spurious effects such as breathing- or motion-induced effects and maximize the filling of the multidimensional space of the data. From the modelling of the changes of the raw k-space data across the cardiac cycle, we estimated the effect of cardiac pulsation on the accuracy and reproducibility of R_2* estimates. The modelled cardiac-induced fluctuations do not distinguish between the physiological processes that may contribute to the effect, but rather represent an overall measure of cardiac-induced noise in R_2*-mapping data. From the distribution of cardiac-induced noise in k-space a tentative strategy to mitigate the effect during data acquisition was presented, which leads to an effective reduction in variability of R_2* maps across repetitions.

The amplitude of cardiac-induced noise increases with the echo time of the data, in line with the expected coupling of spin motion with the gradients of magnetic field used for imaging encoding. This leads to systematic exponential-like effects of cardiac pulsation on the transverse signal decay, and to apparent changes of R_2* across the cardiac cycle. Variations in R_2* of up to 3/2/1/6s^{-1} were observed across the cardiac cycle in the brainstem/cerebellum/whole brain/blood vessels, accounting for 33/38/35/44% of the total variability respectively. Also, the non-exponential effects of cardiac pulsation on the MRI signal leads to an increase of 29/30/30/43% of the noise level of the R_2* estimates in the brainstem/cerebellum/whole brain/blood vessels.

The amplitude of cardiac-induced noise is strongest near the k-space centre and decreases sharply towards the periphery. The improvements in the reproducibility of R_2* maps after detrending the modelled cardiac-induced fluctuations over an increasing fraction of k-space allowed us to delineate the region of k-space sensitive to cardiac-induced noise (Figure 5). We found that this region was within a relatively small radius of 0.0739 mm^{-1} from the k-space centre and contained 25-45% of the total cardiac-induced fluctuations.

The distribution of cardiac-induced noise in k-space is amenable to the design of mitigation strategies that primarily target the k-space centre. Here, we chose to mitigate cardiac-induced noise by restricting data acquisition in the target region to the 1st quarter of the cardiac cycle, where the level of cardiac-induced noise is lowest (see figure 2C). This strategy leads to a decrease in R_2* variability across repetitions of 11%, 8% and 6% in the brainstem, cerebellum and whole-brain, at a cost of 16% scan time increases (Figure 6B). This is more efficient than uninformed averaging methods that would require a scan time increase of ~30% to achieve the same improvements in R_2* reproducibility. The results from the cardiac-gated acquisitions show improved spatial uniformity. In particular, RMSE maps exhibit a reduced level of aliasing of cardiac-induced noise from the circle of Willis along the anterior-posterior direction.

However, the improvements in the stability of R_2* maps with the proposed cardiac gating approach only represent a fraction of the changes in R_2* from the modelled cardiac-induced fluctuations in the five-dimensional datasets. Image resolution in the assessment of the proposed mitigation strategy was higher than the five-dimensional datasets used for the characterization of cardiac-induced noise, leading to a higher contribution of thermal noise to the overall variability of R_2* maps. Also, cardiac-gating was set to act on a restricted area of k-space that contained 25-45% of the total cardiac-induced

noise, leaving a large part of cardiac-induced noise in other k-space regions intact. In particular, blood vessels contain a larger fraction of cardiac-induced noise in high spatial frequencies. The remaining cardiac-induced noise in blood vessels led to a visible amount of spatial aliasing in the data that propagated into the brain (figure 6A, 6C). We highlight that the study of the changes in R_2* maps across the cardiac cycle does not pre-empt spatial aliasing of cardiac-induced noise in routinely acquired images, as this effects arises from differences in cardiac-induced noise level between k-space points.

Visual examination of the maps suggests that head motion may have led to image degradation that partly overshadowed the effects of this noise mitigation strategy. This was confirmed by a quantitative assessment of image quality using a Motion Degradation Index (MDI)[52,60]. Increased MDI values indicative of motion degradation were present in datasets acquired with both standard and cardiac-gated acquisitions. It is therefore likely that head motion might have introduced a substantial contribution to the variability of the R_2* maps between repetitions, leading to a decrease of the relative contribution of cardiac pulsation. The increase in scan time with cardiac gating increases the likelihood of image degradation due to head motion[55,64,65].

5. Conclusion

In this work, we provide a complete assessment of cardiac-induced noise in brain maps of the MRI parameter R_2*. Multi-echo data was acquired at regular intervals across the cardiac cycle using an optimized scheme, enabling the analysis of cardiac pulsation effects on brain R_2* maps. Variations of up to 3/1/6s^{-1} in R_2* were observed across the cardiac cycle in the brainstem/whole brain/blood vessels, accounting for 32/34/44% of the total variability. The amplitude of cardiac-induced noise is strongest near the k-space centre and decreases sharply towards the periphery: the centre 22% of k-space accounts for 37/42/25% of the cardiac-induced fluctuations in the brainstem/whole-brain/blood vessels and 15-20% of the total fluctuations.

The results of the cardiac-induced noise characterization were used to design a mitigation strategy that reduces efficiently the level of cardiac-induced noise in R_2* maps of the brain. The proposed cardiac gating strategy suspends data acquisition during detrimental periods of the cardiac cycle. To minimize the increase in scan time that results from the suspension, cardiac gating was only implemented for the acquisition of the subset of k-space that contains most of the cardiac-induced noise. With the proposed strategy, the variability of R_2* maps was reduced by 11% in the brainstem and 6% across the whole brain, compared to standard acquisition techniques, for an increase in scan time of 13% only.

Data availability statement

The five-dimensional data acquired from one study participant is available online: DOI:10.5281/zenodo.7428605.

The Matlab scripts used for data analysis are available online: DOI:10.5281/zenodo.7446038.

Acknowledgements

The authors thank Dr. Christopher W Roy for his help and insights regarding the sampling strategy, as well as all the participants of the study for their time.

Funding information

This work was supported by the Swiss National Science Foundation (grant no 320030_184784 (AL)) and the Fondation ROGER DE SPOELBERCH. This work was supported by the Swiss National Science Foundation to RBvH (32003B_182615 and CRSII5_202276).

Figures:

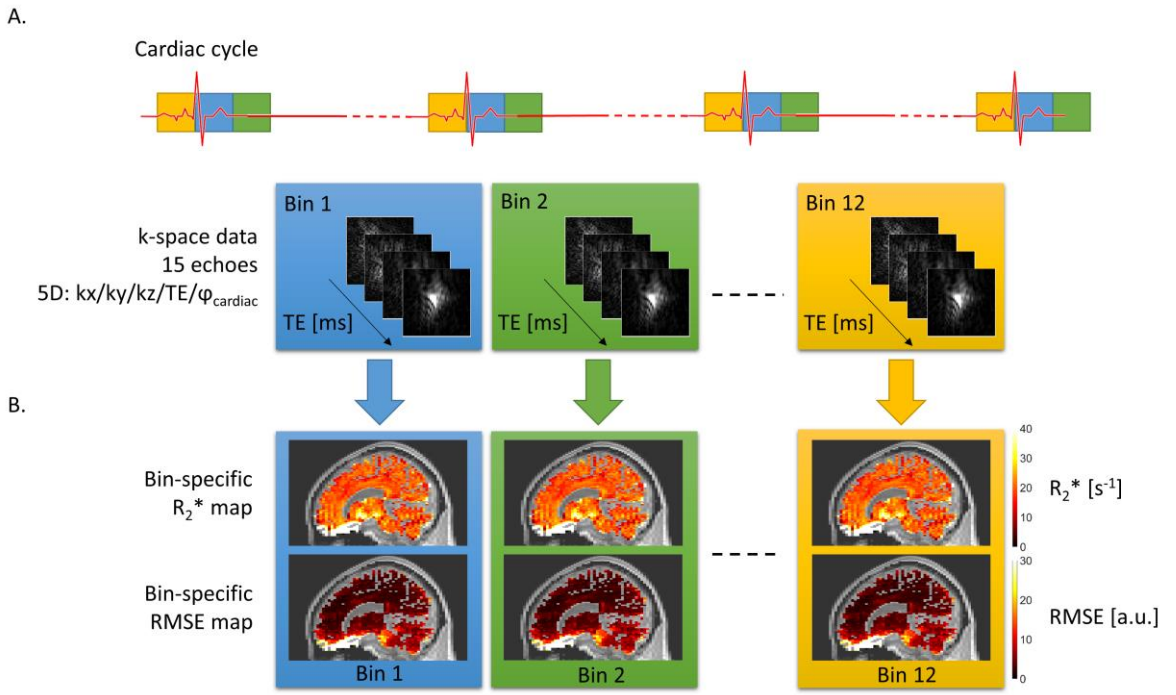

Figure 1: Schematic representation of the acquisition of 5D datasets for the characterization of cardiac-induced noise in brain R_2 maps. (A.) Multi-echo data was acquired continuously for 1 hour while the cardiac rhythm of the participants was recorded using a pulse-oximeter attached to the finger. The data was binned retrospectively according to the phase of the cardiac cycle at the time of its acquisition, leading to k-space datasets with three spatial dimensions (readout and two phase encoding directions), one echo-time dimension and one cardiac phase dimension. (B.) R_2* maps were computed after image reconstruction, from the regression of the log signal with the corresponding echo times. The noise level of the R_2* estimates was calculated as the root-mean-squared error (RMSE) between the MR signal and the R_2* fit.*

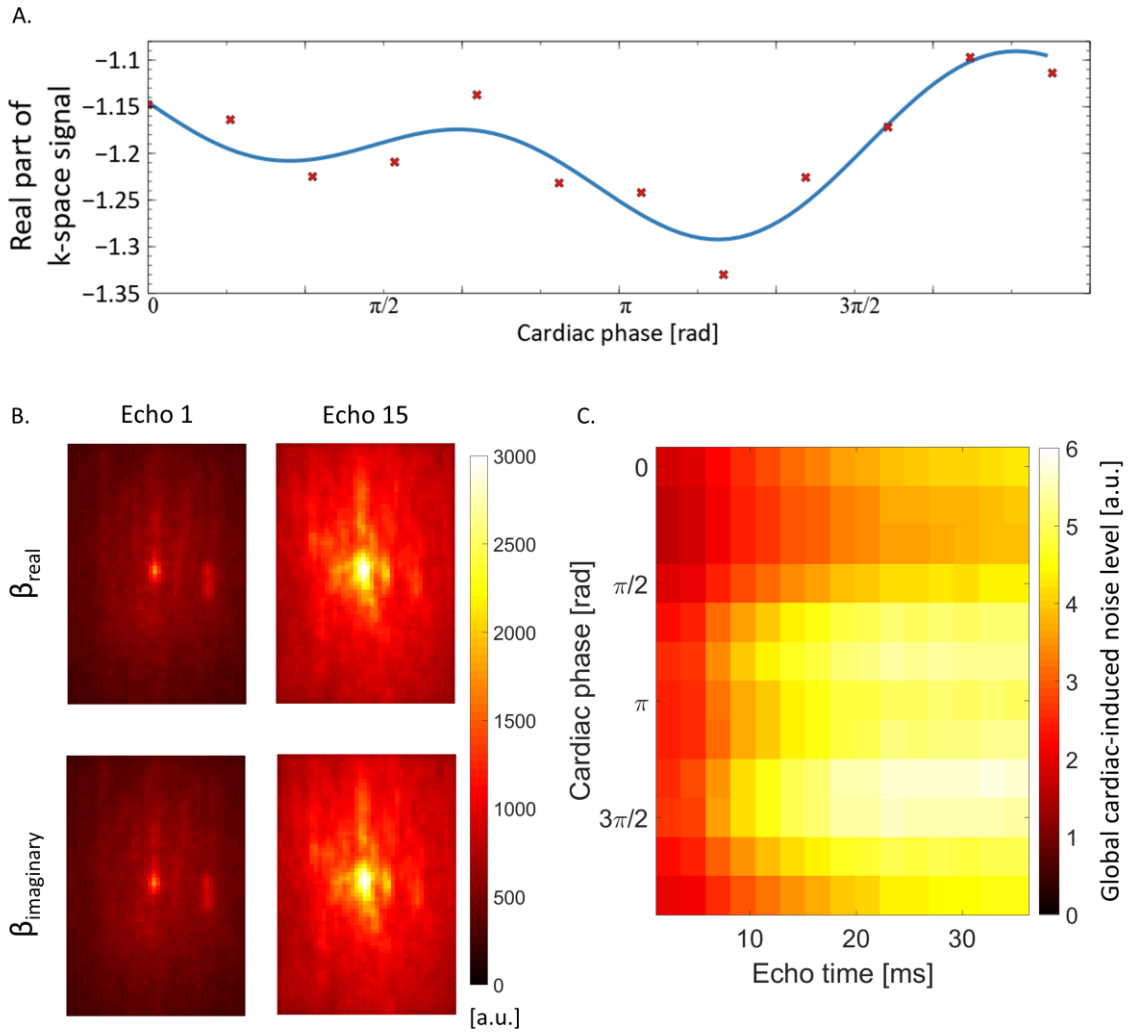

Figure 2: Variations of cardiac-induced noise in R_2 mapping of the brain. (A.) Example fluctuations of the raw signal (red dots) and modelled cardiac-induced noise (blue solid lines) across the cardiac cycle at a given k-space location in the last echo data (TE = 35.10 ms). (B.) K-space distribution of the amplitude of the modelled cardiac-induced fluctuations for the first and last echo data. (C.) Global cardiac-induced noise level as a function of the phase of the cardiac cycle and echo time of the raw MRI data.*

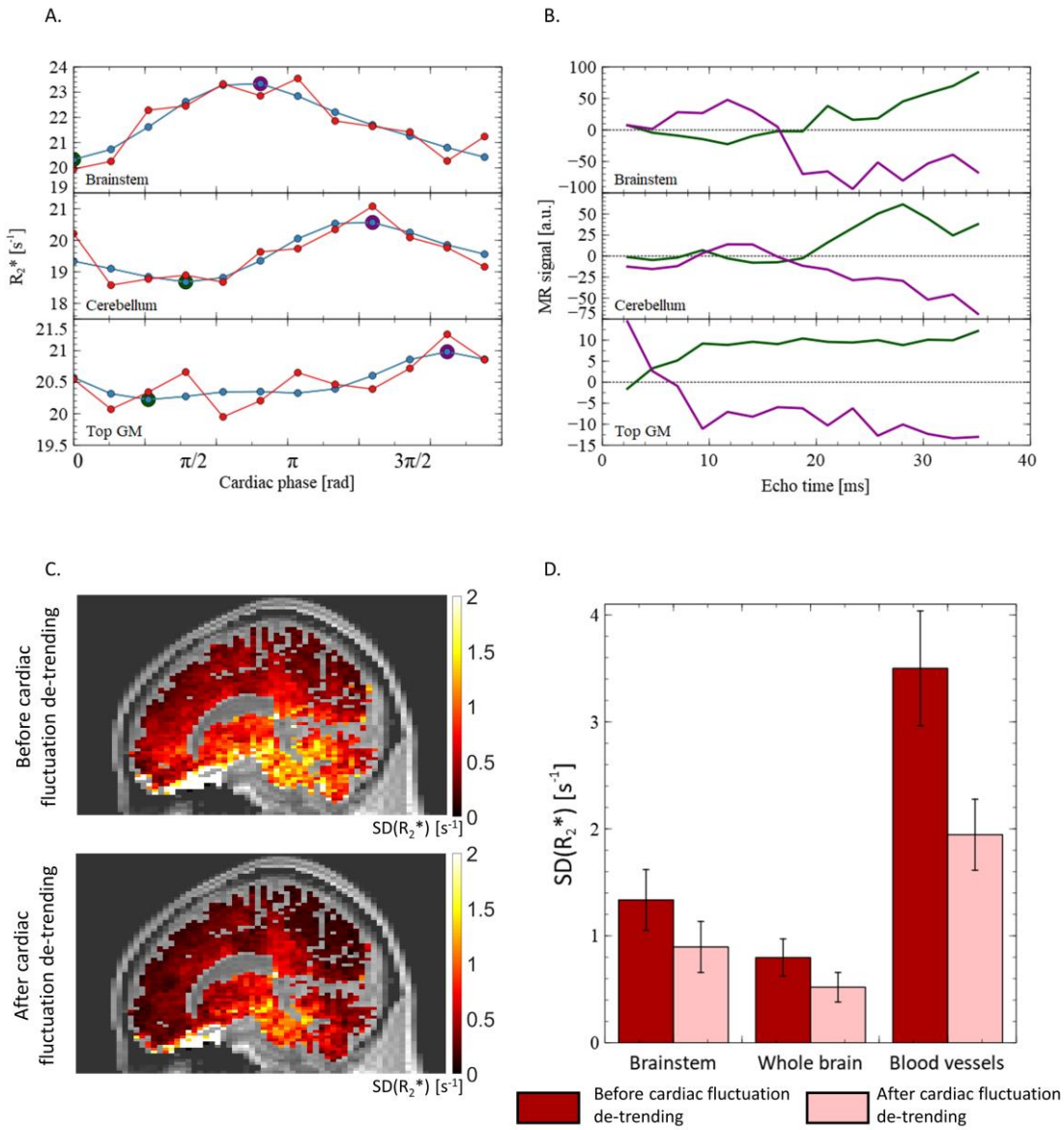

Figure 3: R_2 variability across the cardiac cycle. (A. and B.) Example changes in R_2* across the cardiac cycle in the brainstem, cerebellum and superior cortical grey matter. The changes in the raw data are shown in red and the modelled cardiac-induced changes are shown in blue. The systematic effect of cardiac pulsation on R_2* mirror exponential-like effects on the MRI signal, illustrated in figure 3B for the green and purple data points of figure 3A. (C.) Maps of the standard deviation of R_2* across the cardiac cycle before and after removal of the modelled cardiac-induced noise. (D.) Regional estimates of the standard deviation of R_2* across the cardiac cycle in the brainstem, the whole brain and the blood vessels, averaged across participants.*

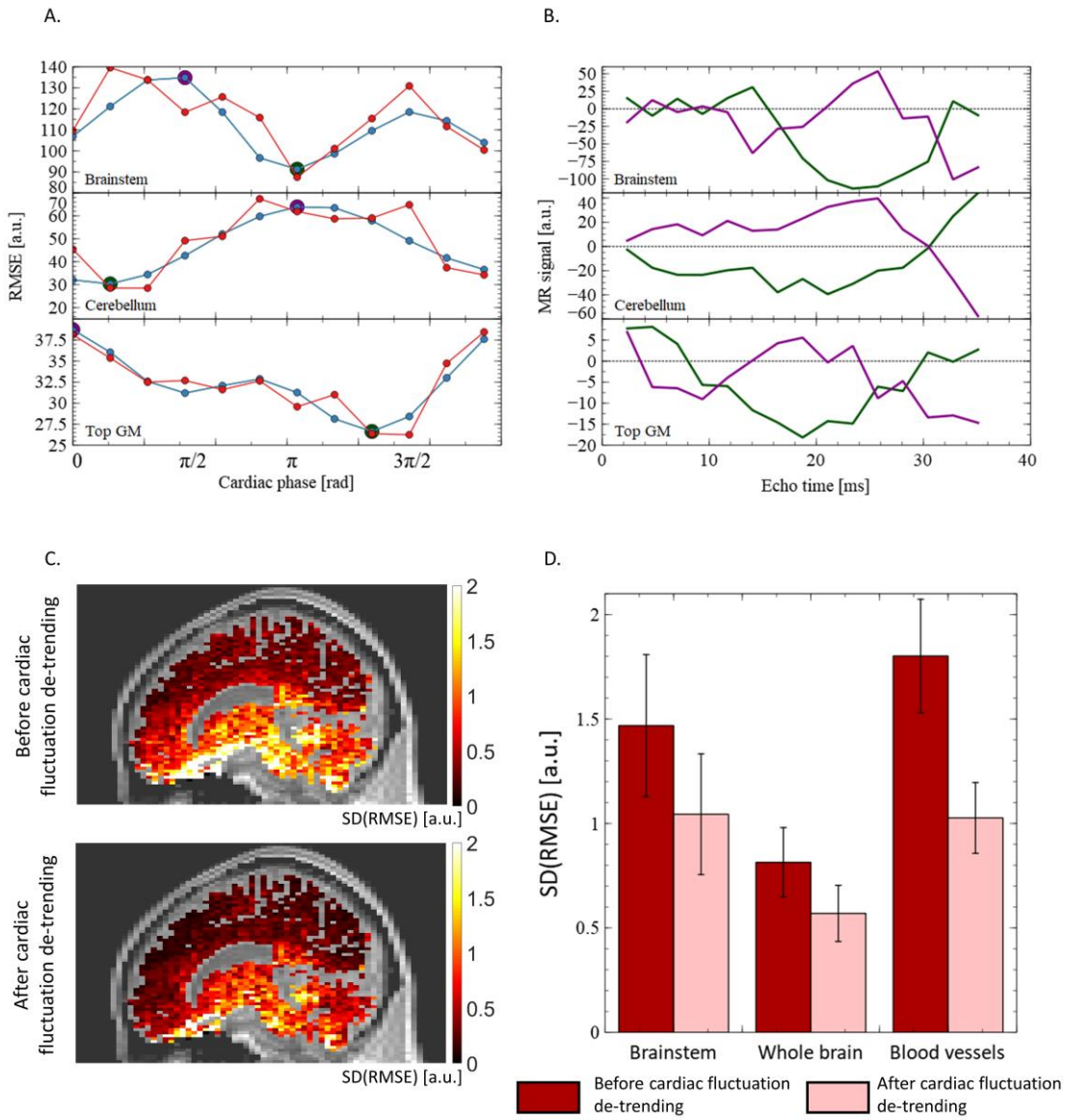

Figure 4: R_2 fit residuals (RMSE) variability across the cardiac cycle. (A. and B.) Example changes in residuals across the cardiac phase in the brainstem, cerebellum and superior cortical grey matter. The changes in the raw data are shown in red and modelled cardiac-induced changes are shown in blue. The deviations of the MRI signal from the mean signal across the cardiac phase is plotted as a function of echo time, for the purple and green points of figure 4A. (C.) Maps of the standard deviation of RMSE across the cardiac cycle before and after removal of the modelled cardiac-induced noise. (D.) Regional estimates of the standard deviation of RMSE across the cardiac cycle in the brainstem, the whole brain, and the blood vessels averaged across participants.*

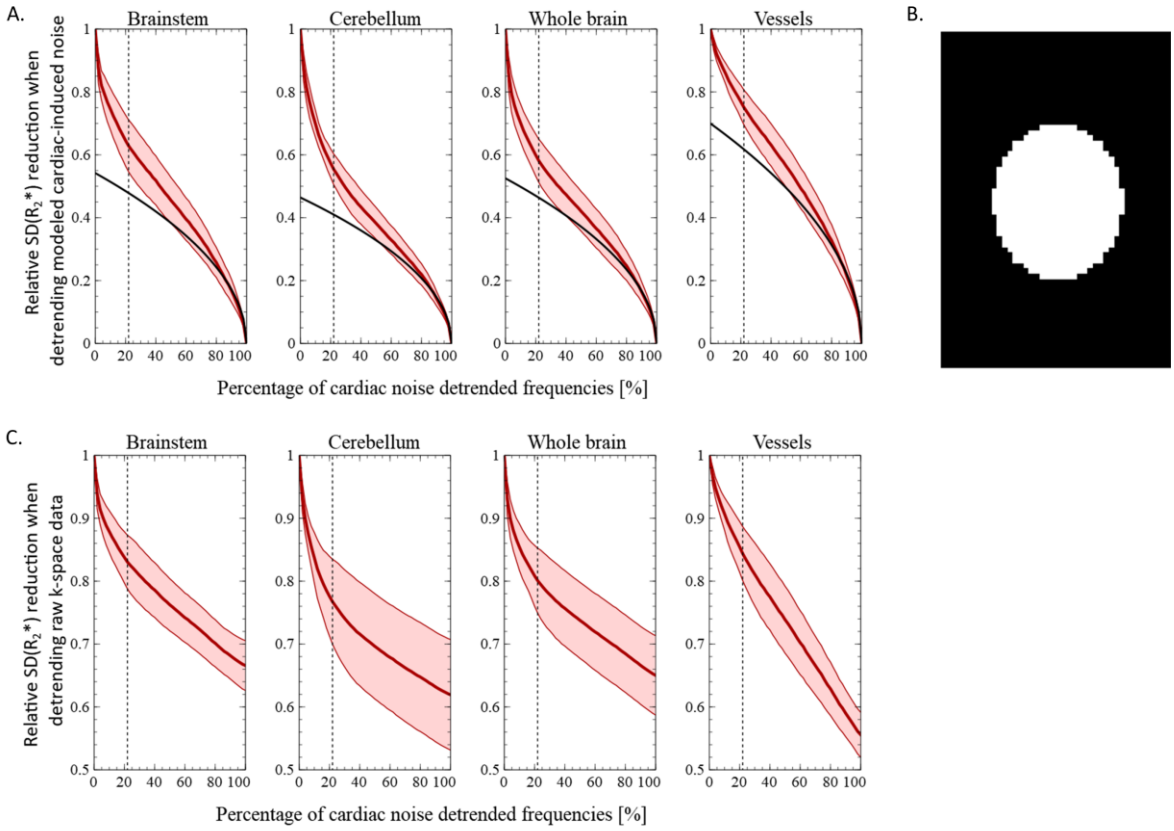

Figure 5: Determination of the k-space regions sensitive to cardiac-induced fluctuations. (A.) Relative standard deviation of R_2 across the cardiac cycle due to the modelled cardiac-induced noise, stripped of its 1st and 2nd-order Fourier components in an increasing fraction of k-space averaged over the brainstem, cerebellum, whole brain and blood vessels for the modelled cardiac-induced noise (red) and uniformly distributed noise (black). The black dotted line correspond the size of the cardiac fluctuation sensitive k-space region. (B.) Sensitive region covering 22% of k-space. (C.) Relative standard deviation of R_2* across the cardiac cycle due in the raw data, stripped of the 1st and 2nd-order Fourier components in an increasing fraction of k-space averaged over the brainstem, cerebellum, whole brain and blood vessels.*

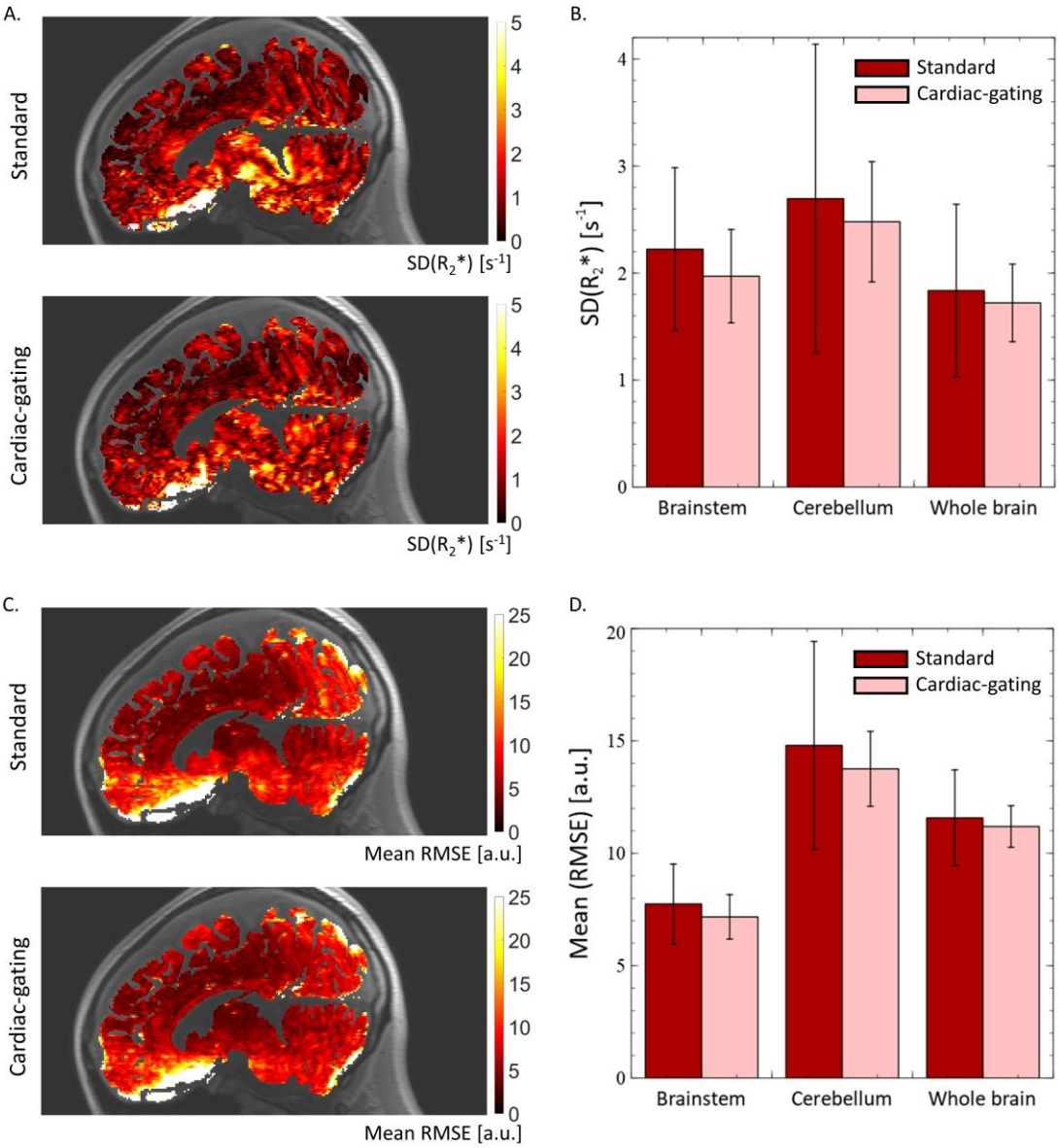

Figure 6: Informed cardiac-induced mitigation strategy. (A.) Example maps of R_2 SD across repetitions for standard and cardiac-gated sequences. (B.) Regional averages of R_2* SD. (C.) Example maps of fit RMSE for standard and cardiac-gated sequences. (D.) Regional averages of RMSE.*

Appendix: Optimizing data acquisition for the characterization of cardiac-induced noise

a. Motivation

30 multi-echo samples were acquired consecutively at each k-space location and cardiac-induced noise was modelled using Fourier series decomposition of the signal change across the cardiac cycle. Figure A1A shows amplitudes of cardiac-induced noise across the cardiac cycle. These results show streaks of 1-4 pixels with high noise amplitude along the fast phase-encode direction, spreading over a duration of up to ~5s during data acquisition. Analysis in image space showed that the source of this effect was primarily located around the mouth and might arise from swallowing.

These results motivated the design of k-space sampling strategies tailored to mitigate spurious, temporally coherent effects (e.g. swallowing, breathing, head motion, scanner drift) while preserving sensitivity to cardiac-induced noise.

b. Strategies for the mitigation of spurious effects

The candidate strategies aimed to distribute spurious effects incoherently across neighbouring k-space locations and were designed around data acquisition within a 2D kernel, i.e. a subset of k-space in the plane of the phase-encode directions. With sampling strategy 1 (Figure A2A), data acquisition is repeated within this kernel before shifting the kernel position by one k-space index along the fast phase-encode direction. With sampling strategy 2 (Figure A2B), the shift of the kernel position takes place after each kernel acquisition and the process is repeated after completing the traversal of k-space along the fast phase-encode direction. Both strategies lead to a total of 30 samples at each k-space location, required for robust estimation of cardiac-induced noise, and data acquisition was conducted for consecutive kernel positions along the slow phase encoding direction (Figure A2C).

Strategy 1 completes data acquisition at each k-space location within a short time window and minimizes low-frequency effects such as scanner drift in the data. However with strategy 1, the mitigation of spurious effects only involves k-space points within the kernel. Strategy 2 allows for a full traversal of k-space along the fast phase-encode direction before repeating data acquisition within a given kernel. Strategy 2 therefore mitigates spurious effects across a larger number of k-space points, at the expense of a longer time window to complete data acquisition at a given k-space location. The time required for the acquisition of 30 samples at each k-space location is shown in Figure A3A. Only kernels with an acquisition below 120s, highlighted in green, were considered to minimize the effect of e.g. scanner drift of head motion.

c. Determination of the optimal mitigation strategy

1. Simulating the occurrence of spurious effects

We conducted numerical simulations to identify the optimal strategy to mitigate spurious effects on the characterization of cardiac-induced noise. Each data point in Figure A1A was labelled as artefact-free or affected by spurious effects using a threshold β value of 5.5. We selected one data point for each label to define template signal variations across the cardiac cycle arising from cardiac-induced and spurious effects (Figure A1B). From these labels, we also computed the successive occurrence of artefact-free and spurious periods in time, given the 2D linear trajectory used to acquire the original data and the 30 repetitions acquired at each k-space location.

From the succession of artefact-free and spurious periods, we simulated a time series of cardiac-induced and spurious signal variations by appropriate sampling of the cardiac and spurious templates. At each time point, the template signals were sampled for a value of the cardiac phase taken from experimental recordings of cardiac pulsation.

In our simulations, this time series of cardiac-induced and spurious signal variations was sampled by the proposed mitigation strategies and distributed across k-space. After completion of the simulated data acquisition, the variation of the acquired data across the cardiac cycle at each k-space location was fitted with Fourier series of sinusoidal basis functions with fundamental and first harmonic.

The efficiency of each mitigation strategy in sampling cardiac-related fluctuations was measured from the percentage of k-space locations with more than 3 empty cardiac bins (Figure A3B). To assess the ability of each mitigation strategy and kernel size to distribute spurious effects, we computed the percentage of k-space locations with more than 3 spurious samples (Figure A3C). The bias induced by spurious effects on the β estimates was computed as the difference between the β estimates obtained from the simulations and the value of β of the original cardiac-induced template (Figure A3D). We verified the homogeneity of the bias of the β estimates induced by spurious effects between k-space points by computing their standard deviation (Figure A3E).

2. Choosing the optimal kernel

With strategy 1, the use of small kernel sizes is equivalent to the acquisition of all 30 samples in each k-space location consecutively: cardiac fluctuations are nearly always sampled for all values of the cardiac phase, but spurious effects are focused on a subset of k-space location, leading to large bias of the β estimates. With increasing kernel size, the mitigation of spurious noise across k-space locations improves (Figure A3C), leading to a lower average bias β estimates with improved homogeneity across k-space (Figure A3D and Figure A3E). Large kernels also allow efficient sampling of cardiac-induced fluctuations (Figure A3B). Sampling strategy 2 leads to better mitigation of spurious noise overall, with a reduced dependence on the kernel size. Specific sets of kernel sizes lead to insufficient sampling of cardiac-induced fluctuations due to synchronization of data acquisition with cardiac pulsation.

From these results, we opted to use sampling strategy 2 with a kernel size of 30 and 2 along the fast and slow phase-encode directions as it represents a good trade-off between the mitigation of spurious effects and efficient sampling of cardiac-induced signal fluctuations.

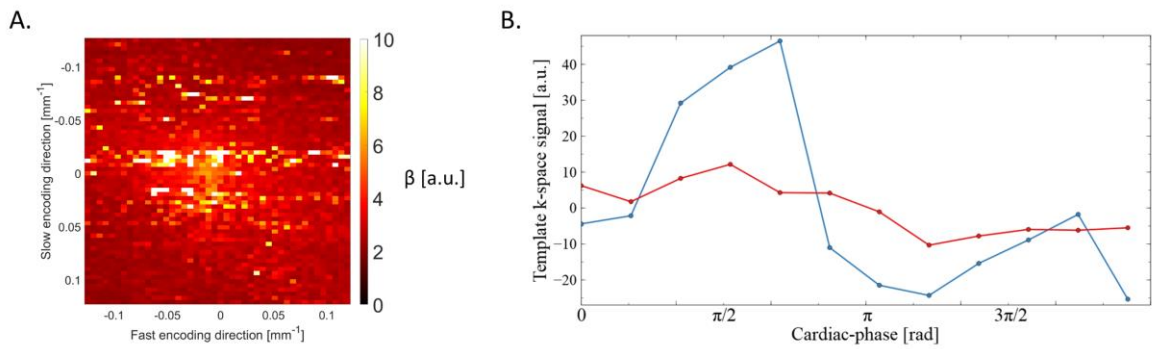

Figure A1: Impact of spurious effect on cardiac-induced noise modeling. (A.) Amplitude of the modeled cardiac-induced noise obtained from 30 data samples acquired consecutively at each k-space location using a 2D linear sampling. The streaks of large β values along the fast encoding direction arise from temporally coherent spurious noise. (B.) Template signal variations across the cardiac cycle due to spurious effects (blue) and cardiac pulsation (red).

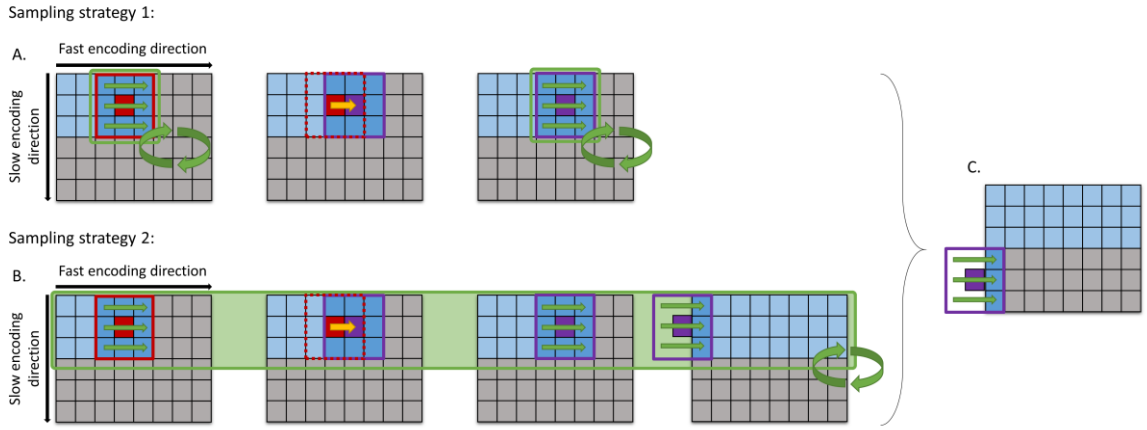

Figure A2: Schematic representation of the kernel displacements in k-space for the two sampling strategies. (A.) Sampling strategy 1 repeats data acquisition within the kernel several times before shifting the kernel position by one k-space index along the fast phase-encode direction. (B.) Sampling strategy 2 shift the kernel position after each kernel acquisition and the process is repeated after completing the traversal of k-space along the fast phase-encode direction. (C.) Both strategies lead to a total of 30 samples at each k-space location, and data acquisition was conducted for consecutive kernel positions along the slow phase encoding direction.

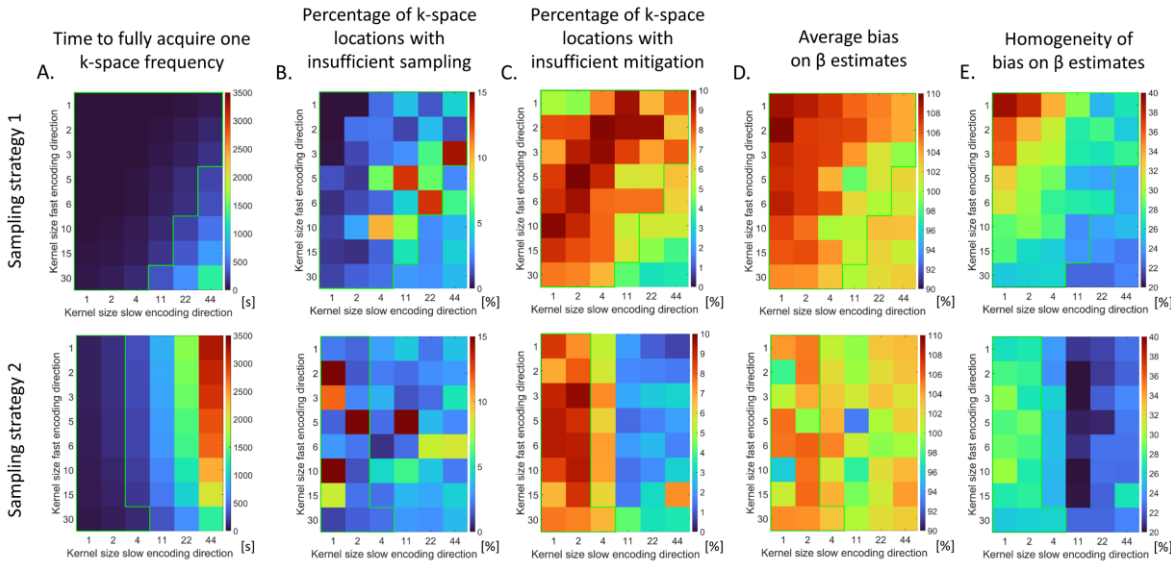

Figure A3: Evaluation of the sampling strategies 1 and 2. (A.) Time of acquisition of 30 samples at each k-space location. Only kernels with an acquisition time below 120s, highlighted in green, were considered. (B.) Percentage of k-space locations with insufficient sampling (i.e. more than 3 empty cardiac bins) (C.) Percentage of k-space locations with insufficient spurious effect mitigation (i.e. more than 3 spurious samples). (D.) Average bias on the β estimates induced by spurious effects. (E.) Homogeneity of the bias on the β estimates across k-space locations.

References

1. Deoni SCL. Quantitative Relaxometry of the Brain. *J Rehabil*. 2010;78(3):20-26. doi:10.1097/RMR.0b013e31821e56d8.Quantitative

2. Tabelow K, Balteau E, Ashburner J, et al. hMRI – A toolbox for quantitative MRI in neuroscience and clinical research. *Neuroimage*. 2019;194(September 2018):191-210. doi:10.1016/j.neuroimage.2019.01.029

3. Weiskopf N, Edwards LJ, Helms G, Mohammadi S, Kirilina E. Quantitative magnetic resonance imaging of brain anatomy and in vivo histology. *Nat Rev Phys*. 2021;3(8):570-588. doi:10.1038/s42254-021-00326-1

4. Weiskopf N, Suckling J, Williams G, et al. Quantitative multi-parameter mapping of R1, PD*, MT, and R2* at 3T: A multi-center validation. *Front Neurosci*. 2013;7(7 JUN):1-11. doi:10.3389/fnins.2013.00095

5. Leutritz T, Seif M, Helms G, et al. Multiparameter mapping of relaxation (R1, R2*), proton density and magnetization transfer saturation at 3 T: A multicenter dual-vendor reproducibility and repeatability study. *Hum Brain Mapp*. 2020;41(15):4232-4247. doi:10.1002/hbm.25122

6. Chavhan GB, Babyn PS, Thomas B, Shroff MM, Mark Haacke E. Principles, techniques, and applications of T2*-based MR imaging and its special applications. *Radiographics*. 2009;29(5):1433-1449. doi:10.1148/rg.295095034

7. Novikov DS, Kiselev VG, Jespersen SN. On modeling. *Magn Reson Med*. 2018;79(6):3172-3193. doi:10.1002/mrm.27101

8. Fukunaga M, Li TQ, Van Gelderen P, et al. Layer-specific variation of iron content in cerebral cortex as a source of MRI contrast. *Proc Natl Acad Sci U S A*. 2010;107(8):3834-3839. doi:10.1073/pnas.0911177107

9. Cohen-Adad J. What can we learn from T2* maps of the cortex? *Neuroimage*. 2014;93:189-200. doi:10.1016/j.neuroimage.2013.01.023

10. Stüber C, Morawski M, Schäfer A, et al. Myelin and iron concentration in the human brain: A quantitative study of MRI contrast. *Neuroimage*. 2014;93(P1):95-106. doi:10.1016/j.neuroimage.2014.02.026

11. Haacke EM, Cheng NYC, House MJ, et al. Imaging iron stores in the brain using magnetic resonance imaging. *Magn Reson Imaging*. 2005;23(1):1-25. doi:10.1016/j.mri.2004.10.001

12. Barbosa JHO, Santos AC, Tumas V, et al. Quantifying brain iron deposition in patients with Parkinson's disease using quantitative susceptibility mapping, R2 and R2*. *Magn Reson Imaging*. 2015;33(5):559-565. doi:10.1016/j.mri.2015.02.021

13. Ulla M, Bonny JM, Ouchchane L, Rieu I, Claise B, Durif F. Is R2* a New MRI Biomarker for the Progression of Parkinson's Disease? A Longitudinal Follow-Up. *PLoS One*. 2013;8(3):1-8. doi:10.1371/journal.pone.0057904

14. Khalil M, Enzinger C, Langkammer C, et al. Quantitative assessment of brain iron by R2* relaxometry in patients with clinically isolated syndrome and relapsing-remitting multiple sclerosis. *Mult Scler*. 2009;15(9):1048-1054. doi:10.1177/1352458509106609

15. Langkammer C, Ropele S, Pirpamer L, Fazekas F, Schmidt R. MRI for iron mapping in Alzheimer's disease. *Neurodegener Dis*. 2014;13(2-3):189-191. doi:10.1159/000353756

16. El Sankari S, Gondry-Jouet C, Fichten A, et al. Cerebrospinal fluid and blood flow in mild cognitive impairment and Alzheimer's disease: A differential diagnosis from idiopathic normal pressure hydrocephalus. *Fluids Barriers CNS*. 2011;8(1). doi:10.1186/2045-8118-8-12

17. Schnell S, Wu C, Ansari SA. 4D MRI flow examinations in cerebral and extracerebral vessels. Ready for clinical routine? HHS Public Access. *Curr Opin Neurol*. 2016;29(4):419-428. doi:10.1097/WCO.0000000000000341.4D

18. Skare S, Andersson JLR. On the effects of gating in diffusion imaging of the brain using single shot EPI. *Magn Reson Imaging*. 2001;19(8):1125-1128. doi:10.1016/S0730-725X(01)00415-5

19. Nunes RG, Jezzard P, Clare S. Investigations on the efficiency of cardiac-gated methods for the acquisition of diffusion-weighted images. *J Magn Reson*. 2005;177(1):102-110. doi:10.1016/j.jmr.2005.07.005

20. Pierpaoli C, Marenco S, Rohde GK, Jones DK, Barnett a S. Analyzing the contribution of cardiac pulsation to the variability of quantities derived from the diffusion tensor. *Proc ISMRM 11th Sci Meet Exhib*. 2003;11:70.

21. Bianciardi M, Toschi N, Polimeni JR, et al. The pulsatility volume index: An indicator of cerebrovascular compliance based on fast magnetic resonance imaging of cardiac and respiratory pulsatility. *Philos Trans R Soc A Math Phys Eng Sci*. 2016;374(2067). doi:10.1098/rsta.2015.0184

22. Morgan AG, Thrippleton MJ, Wardlaw JM, Marshall I. 4D flow MRI for non-invasive measurement of blood flow in the brain: A systematic review. *J Cereb Blood Flow Metab*. 2021;41(2):206-218. doi:10.1177/0271678X20952014

23. Tao Y, Rilling G, Davies M, Marshall I. Carotid blood flow measurement accelerated by compressed sensing: Validation in healthy volunteers. *Magn Reson Imaging*. 2013;31(9):1485-1491. doi:10.1016/j.mri.2013.05.009

24. Schuchardt F, Schroeder L, Anastasopoulos C, et al. In vivo analysis of physiological 3D blood flow of cerebral veins. *Eur Radiol*. 2015;25(8):2371-2380. doi:10.1007/s00330-014-3587-x

25. Zhong X, Meyer CH, Schlesinger DJ, et al. Tracking brain motion during the cardiac cycle using spiral cine-DENSE MRI. *Med Phys*. 2009;36(8):3413-3419. doi:10.1118/1.3157109

26. Soellinger M, Rutz AK, Kozerke S, Boesiger P. 3D cine displacement-encoded MRI of pulsatile brain motion. *Magn Reson Med*. 2009;61(1):153-162. doi:10.1002/mrm.21802

27. Sloots JJ, Froeling M, Biessels GJ, Zwanenburg JJM. Dynamic brain ADC variations over the cardiac cycle and their relation to tissue strain assessed with DENSE at high-field MRI. *Magn Reson Med*. 2022;88(1):266-279. doi:10.1002/mrm.29209

28. Sloots JJ, Biessels GJ, de Luca A, Zwanenburg JJM. Strain Tensor Imaging: Cardiac-induced brain tissue deformation in humans quantified with high-field MRI. *Neuroimage*. 2021;236(April):118078. doi:10.1016/j.neuroimage.2021.118078

29. Chen L, Beckett A, Verma A, Feinberg DA. Dynamics of respiratory and cardiac CSF motion revealed with real-time simultaneous multi-slice EPI velocity phase contrast imaging. *Neuroimage*. 2015;122:281-287. doi:10.1016/j.neuroimage.2015.07.073

30. Beissner F. Functional MRI of the Brainstem: Common Problems and their Solutions. *Clin Neuroradiol*. 2015;25:251-257. doi:10.1007/s00062-015-0404-0

31. Hermes D, Wu H, Kerr AB, Wandell BA. Measuring brain beats: Cardiac-aligned fast functional magnetic resonance imaging signals. *Hum Brain Mapp*. 2022. doi:10.1002/hbm.26128

32. Maclaren J, Armstrong BSR, Barrows RT, et al. Measurement and Correction of Microscopic Head Motion during Magnetic Resonance Imaging of the Brain. *PLoS One*. 2012;7(11):3-11. doi:10.1371/journal.pone.0048088

33. Petridou N, Schäfer A, Gowland P, Bowtell R. Phase vs. magnitude information in functional magnetic resonance imaging time series: toward understanding the noise. *Magn Reson Imaging*. 2009;27(8):1046-1057. doi:10.1016/j.mri.2009.02.006

34. Menon RS. Postacquisition suppression of large-vessel BOLD signals in high-resolution fMRI. *Magn Reson Med*. 2002;47(1):1-9. doi:10.1002/mrm.10041

35. Brooks JCW, Faull OK, Pattinson KTS, Jenkinson M. Physiological noise in brainstem fMRI. *Front Hum Neurosci*. 2013;c(OCT):1-13. doi:10.3389/fnhum.2013.00623

36. van der Zwaag W, Jorge J, Butticaz D, Gruetter R. Physiological noise in human cerebellar fMRI. *Magn Reson Mater Physics, Biol Med*. 2015;28(5):485-492. doi:10.1007/s10334-015-0483-6

37. Dagli MS, Ingeholm JE, Haxby J V. Localization of cardiac-induced signal change in fMRI. *Neuroimage*. 1999;9(4):407-415. doi:10.1006/nimg.1998.0424

38. Deckers RHR, van Gelderen P, Ries M, et al. An adaptive filter for suppression of cardiac and respiratory noise in MRI time series data. *Neuroimage*. 2006;33(4):1072-1081. doi:10.1016/j.neuroimage.2006.08.006

39. Xu B, Liu T, Spincemaille P, Prince M, Wang Y. Flow compensated quantitative susceptibility mapping for venous oxygenation imaging. *Magn Reson Med*. 2014;72(2):438-445. doi:10.1002/mrm.24937

40. Glover GH, Li TQ, Ress D. Image-based method for retrospective correction of physiological motion effects in fMRI: RETROICOR. *Magn Reson Med*. 2000;44(1):162-167. doi:10.1002/1522-2594(200007)44:1<162::AID-MRM23>3.0.CO;2-E

41. Tijssen RHN, Jenkinson M, Brooks JCW, Jezzard P, Miller KL. Optimizing RetroICor and RetroKCor corrections for multi-shot 3D FMRI acquisitions. *Neuroimage*. 2014;84:394-405. doi:10.1016/j.neuroimage.2013.08.062

42. Agrawal U, Brown EN, Lewis LD. Model-based physiological noise removal in fast fMRI. *Neuroimage*. 2020;205(September 2019):116231. doi:10.1016/j.neuroimage.2019.116231

43. Mohammadi S, Hutton C, Nagy Z, Josephs O, Weiskopf N. Retrospective correction of physiological noise in DTI using an extended tensor model and peripheral measurements. *Magn Reson Med*. 2013;70(2):358-369. doi:10.1002/mrm.24467

44. Tijssen RHN, Okell TW, Miller KL. Real-time cardiac synchronization with fixed volume frame rate for reducing physiological instabilities in 3D FMRI. *Neuroimage*. 2011;57(4):1364-1375. doi:10.1016/j.neuroimage.2011.05.070

45. Kristoffersen A, Goa PE. Cardiac-induced physiological noise in 3D gradient echo brain imaging: Effect of k-space sampling scheme. *J Magn Reson*. 2011;212(1):74-85. doi:10.1016/j.jmr.2011.06.012

46. Feng L, Coppo S, Piccini D, et al. 5D whole-heart sparse MRI. *Magn Reson Med*. 2018;79(2):826-838. doi:10.1002/mrm.26745

47. Coppo S, Piccini D, Bonanno G, et al. Free-running 4D whole-heart self-navigated golden angle MRI: Initial results. *Magn Reson Med*. 2015;74(5):1306-1316. doi:10.1002/mrm.25523

48. Di Sopra L, Piccini D, Coppo S, Stuber M, Yerly J. An automated approach to fully self-gated free-running cardiac and respiratory motion-resolved 5D whole-heart MRI. *Magn Reson Med*. 2019;82(6):2118-2132. doi:10.1002/mrm.27898

49. Markl M, Schnell S, Wu C, et al. Advanced flow MRI: emerging techniques and applications. *Clin Radiol*. 2016;71(8):779-795. doi:10.1016/j.crad.2016.01.011

50. Pruessmann KP, Weiger M, Scheidegger MB, Boesiger P. SENSE: Sensitivity encoding for fast MRI. *Magn Reson Med*. 1999;42(5):952-962. doi:10.1002/(SICI)1522-2594(199911)42:5<952::AID-MRM16>3.0.CO;2-S

51. Weiskopf N, Callaghan MF, Josephs O, Lutti A, Mohammadi S. Estimating the apparent transverse relaxation time (R2*) from images with different contrasts (ESTATICS) reduces motion artifacts. *Front Neurosci*. 2014;8(SEP):1-10. doi:10.3389/fnins.2014.00278

52. Castella R, Arn L, Dupuis E, Callaghan MF, Draganski B, Lutti A. Controlling motion artefact levels in MR images by suspending data acquisition during periods of head motion. *Magn Reson Med*. 2018;80(6):2415-2426. doi:10.1002/mrm.27214

53. Mugler JP, Brookeman JR. Three-dimensional magnetization-prepared rapid gradient-echo imaging (3D MP RAGE). *Magn Reson Med*. 1990;15(1):152-157. doi:10.1002/mrm.1910150117

54. Griswold MA, Jakob PM, Heidemann RM, et al. Generalized Autocalibrating Partially Parallel Acquisitions (GRAPPA). *Magn Reson Med*. 2002;47(6):1202-1210. doi:10.1002/mrm.10171

55. Papp D, Callaghan MF, Meyer H, Buckley C, Weiskopf N. Correction of inter-scan motion artifacts in quantitative R1 mapping by accounting for receive coil sensitivity effects. *Magn Reson Med*. 2016;76(5):1478-1485. doi:10.1002/mrm.26058

56. Péran P, Hagberg G, Luccichenti G, et al. Voxel-based analysis of R2* maps in the healthy human brain. *J Magn Reson Imaging*. 2007;26(6):1413-1420. doi:10.1002/jmri.21204

57. Ghadery C, Pirpamer L, Hofer E, et al. R2* mapping for brain iron: Associations with cognition in normal aging. *Neurobiol Aging*. 2015;36(2):925-932. doi:10.1016/j.neurobiolaging.2014.09.013

58. Callaghan MF, Freund P, Draganski B, et al. Widespread age-related differences in the human brain microstructure revealed by quantitative magnetic resonance imaging. *Neurobiol Aging*. 2014;35(8):1862-1872. doi:10.1016/j.neurobiolaging.2014.02.008

59. Ashburner J, Friston KJ. Unified segmentation. *Neuroimage*. 2005;26(3):839-851. doi:10.1016/j.neuroimage.2005.02.018

60. Lutti A, Corbin N, Ashburner J, et al. Restoring statistical validity in group analyses of motion-corrupted MRI data. *Hum Brain Mapp*. 2022;43(6):1973-1983. doi:10.1002/hbm.25767

61. Hutter J, Schmitt P, Saake M, et al. Multi-dimensional flow-preserving compressed sensing (MuFloCoS) for time-resolved velocity-encoded phase contrast MRI. *IEEE Trans Med Imaging*. 2015;34(2):400-414. doi:10.1109/TMI.2014.2359238

62. Friedman L, Glover GH. Report on a multicenter fMRI quality assurance protocol. *J Magn Reson Imaging*. 2006;23(6):827-839. doi:10.1002/jmri.20583

63. Satopää V, Albrecht J, Irwin D, Raghavan B. Finding a “kneedle” in a haystack: Detecting knee points in system behavior. *Proc - Int Conf Distrib Comput Syst*. 2011:166-171. doi:10.1109/ICDCSW.2011.20

64. Menon V, Lim KO, Anderson JH, Johnson J, Pfefferbaum A. Design and efficacy of a head-coil

bite bar for reducing movement-related artifacts during functional MRI scanning. *Behav Res Methods, Instruments, Comput*. 1997;29(4):589-594. doi:10.3758/BF03210613

65. Krause F, Benjamins C, Eck J, Lührs M, van Hoof R, Goebel R. Active head motion reduction in magnetic resonance imaging using tactile feedback. *Hum Brain Mapp*. 2019;40(14):4026-4037. doi:10.1002/hbm.24683